Comparison of angle decomposition methods for wave-equation migration

Natalya Patrikeeva and Paul Sava, Center for Wave Phenomena, Colorado School of Mines*

SUMMARY

Angle domain common image gathers offer advantages for subsurface image analysis in complex media. We compare two angle decomposition methods using extended images and wave propagation directions based on Poynting vectors of the source and receiver wavefields. We evaluate the ability of each method to produce accurate and efficient angle gathers for wave-equation migration in the presence of multi-arrivals and in the subsalt environment. Both methods are characterized by features that make them attractive in different situations.

INTRODUCTION

Common image gathers (CIGs) produced by Kirchhoff migration are often used for tomographic subsalt velocity updates. However, these gathers suffer from artifacts induced by multipathing and by poor subsalt data quality. To address these problems, subsurface angle gathers can be constructed from non-ray based migrations such as reverse time migration (RTM) and wave equation migration (WEM). Wave-equation migration properly handles multiple propagation paths and produces accurate images in complex environments as opposed to Kirchhoff migration (Gray et al., 2001).

Migrated images partitioned based on the reflection and azimuth angles characterize the reflector illumination in the subsurface and provide information for migration velocity analysis (MVA) and amplitude variation with angle (AVA) (de Bruin et al., 1990; Prucha et al., 1999; Sava et al., 2001; Fomel, 2004; Biondi and Symes, 2004)). Subsurface angle gathers avoid some imaging artifacts and improve migration velocity updates by reducing the impact of multipathing associated with the offset-domain CIGs.

Different techniques have been proposed to address the problem of angle-domain imaging in complex geologic structures. Generally speaking, we can separate these techniques into two categories: techniques based on decomposition of wavefields prior to the imaging condition, and techniques based on decomposition of migrated images after the imaging condition. Although they share a common objective, the techniques in the two categories have significant differences in quality and computational cost.

In this abstract, we describe two methods capable of constructing subsurface angle gathers and compare them from the perspectives of cost, accuracy and applicability to imaging in complex media. The first considered method uses decomposition of extended images – the EI method (Rickett and Sava, 2002; Sava and Fomel, 2003, 2005; Sava and Vlad, 2011a; Fomel, 2011), and the second method uses decomposition of extrapolated vectors using Poynting vectors – the PV method (Yoon and Marfurt, 2004; Yoon et al., 2011; Vyas et al., 2011; Dickens and Winbow, 2011; Crawley et al., 2012). Both methods use seismic wavefields reconstructed by reverse-time extrapolation or by downward continuation. We assume that we compare similar outputs, i.e. angle-gathers computed at all locations in space, although as indicated by Sava and Vasconcelos (2011) this is not an efficient approach.

ANGLE DECOMPOSITION

A conventional cross-correlation imaging condition for wave-equation migration is (Claerbout, 1985)

$$R(\mathbf{x}) = \sum_e \sum_t W_r(e,\mathbf{x},t)\, W_s(e,\mathbf{x},t)\,, \qquad (1)$$

where $\mathbf{x} = \{x, y, z\}$ are space coordinates, W_s and W_r are the source and receiver wavefields, e is the experiment (shot) index, t is time, and $R(\mathbf{x})$ is the migrated image.

The conventional imaging condition is a special case of the generalized or extended imaging condition (Sava and Fomel, 2005):

$$R(\mathbf{x},\boldsymbol{\lambda},\tau) = \sum_e \sum_t W_s(e,\mathbf{x}-\boldsymbol{\lambda},t-\tau)\, W_r(e,\mathbf{x}+\boldsymbol{\lambda},t+\tau)\,, \qquad (2)$$

where $\boldsymbol{\lambda} = \{\lambda_x, \lambda_y, \lambda_z\}$ are the cross-correlation space lags, τ is the cross-correlation time lag, and $R(\mathbf{x},\boldsymbol{\lambda},\tau)$ is the extended image. The conventional imaging condition, equation 1, is a special case of the extended imaging condition, equation 2, when $\boldsymbol{\lambda} = \mathbf{0}$ and $\tau = 0$.

In this paper we consider a special case of the extended images for $\tau = 0$, i.e. we discuss space-lag gathers. This extended imaging condition produces migrated images as a function of space $\mathbf{x}$ and a local subsurface offset $\boldsymbol{\lambda}$. The space-lag between the wavefields can be converted to the reflection and azimuth angles at each image point using a local slant-stack, or equivalently, a radial-trace transform (Fomel, 1997; Sava and Fomel, 2000; Rickett and Sava, 2002; Sava and Fomel, 2003). This decomposition method assumes a smooth velocity field near the image point, thus justifying the local slant-stack. This operation is performed in extended common-image gathers (CIGs), although a more efficient implementation takes advantage of common-image-point gathers (CIPs) (Sava and Vlad, 2011b). Algorithm 1 summarizes the method used to convert the extended images to angle gathers.

Yoon and Marfurt (2004) propose a method to compute angle gathers during reverse time migration (RTM) via a

Poynting vector imaging condition. They use the Poynting vector to compute the opening angle between the source and receiver directions and filter the RTM backscattered energy artifacts. Other authors follow their method to output angle gathers as a product of migration (Vyas et al. (2011); Yoon et al. (2011); Dickens and Winbow (2011); Crawley et al. (2012)).

Yoon and Marfurt (2004) calculate Poynting vectors as a product of the time derivative and the gradient of the wavefield. This method requires accurate numerical derivatives to produce correct angles and access to multiple time steps during wavefield extrapolation, which is not always practical for time extrapolation methods like RTM. Alternatively, we can construct the Poynting vectors for acoustic waves as a product of pressure and particle velocity (Kaufman et al., 2002):

$$\mathbf{P}\left(e,\mathbf{x},t\right)=W\left(e,\mathbf{x},t\right)\boldsymbol{V}\left(e,\mathbf{x},t\right)\ , \tag{3}$$

where $\mathbf{P}$ is the Poynting vector, W is the pressure wavefield, and $\boldsymbol{V}$ is the particle velocity.

By definition, the Poynting vector is the energy flux density vector. Its magnitude defines the amount of energy transmitted through the unit area per unit time. In the high frequency approximation, the Poynting vector is oriented along the ray, i.e. it captures the group velocity angle in general anisotropic media. Here we use the Poynting vector to define the propagation directions of the source and receiver wavefields. Then, we can define the reflection and azimuth angles as

$$\sin\left(2\theta\right)=\frac{\left(\mathbf{P}_s\times\mathbf{P}_r\right)\cdot\hat{\mathbf{k}}}{|\mathbf{P}_s||\mathbf{P}_r|}\ ,\sin\left(2\phi\right)=\frac{\left(\mathbf{P}_r-\mathbf{P}_s\right)\cdot\hat{\mathbf{k}}}{||\mathbf{P}_r-\mathbf{P}_s||}\ , \tag{4}$$

where $\mathbf{P}_s\left(e,\mathbf{x},t\right)$ and $\mathbf{P}_r\left(e,\mathbf{x},t\right)$ are the Poynting vectors of the source and receiver wavefields, respectively, and $\hat{\mathbf{k}}$ is the unit vector along the z axis. The values of the reflection angle range from -90^o to $+90^o$. Using the cross product instead of the dot product of the two Poynting vectors allows us to differentiate between negative and positive values of reflection angle θ. Algorithm 2 outlines the angle decomposition method using Poynting vectors of the source and receiver wavefields. After we calculate the angles, we map the image contribution to the appropriate angle bin.

The Poynting vectors oscillate rapidly since they are highly sensitive to noise present in the extrapolated wavefields. This noise could either originate in the data, or it could be the result of interference between waves propagating in different directions. Therefore, reliable Poynting vectors require spatial and/or temporal smoothing before the angle calculations in order to reduce their rapid spatial and temporal oscillations which degrade angle calculation. For example, Yoon et al. (2011) average the Poynting vector over four periods of the source wavelet, and Dickens and Winbow (2011) smooth the vector components over a small region in space. We use similar space and time smoothing in our examples. The downside of this operation is that the accuracy of

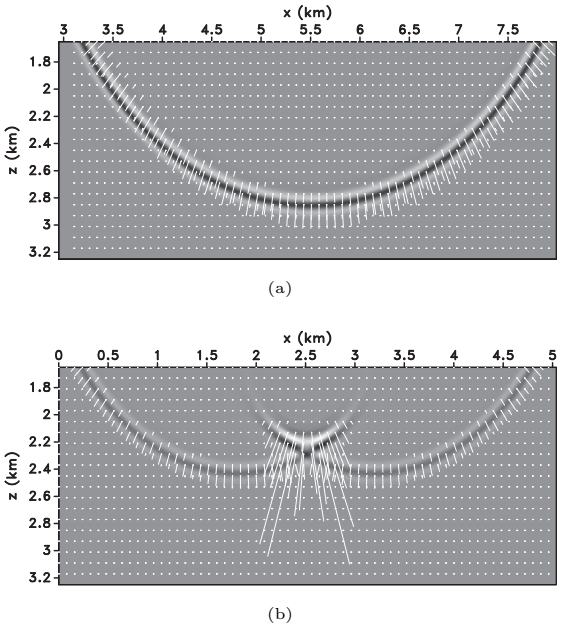

Figure 1: Poynting vectors represented on wavefields (a) in a constant medium and (b) in a medium with a negative Gaussian anomaly.

the Poynting vector direction degrades, especially in areas of high wavefield complexity like sub-salt. Furthermore, if different wavefield components interfere, e.g. at triplications, then the Poynting vector captures an average direction which does not represent either of the branches of the reconstructed wavefield, thus degrading angle-domain accuracy.

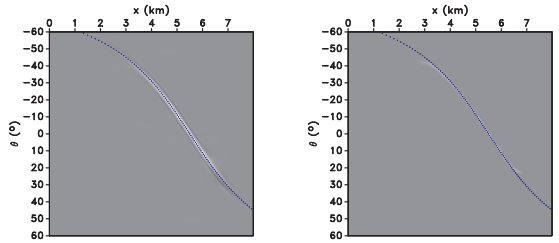

Figure 2: Reflection angles computed on a horizontal reflector in constant velocity using the EI and the PV methods. The overlay depicts the theoretical reflection angles along the horizontal reflector.

Figure 1 illustrates the behavior of Poynting vectors for simple wavefields (a) and for complex wavefields (b) due to a negative velocity anomaly. The vectors accurately describe the propagation directions in simple media but do not achieve the same accuracy and reliability in complex media. Nevertheless, if the medium is fairly simple, then both methods based on extended images (EI) and Poynting vectors (PV) lead to accurate angles, as illus-

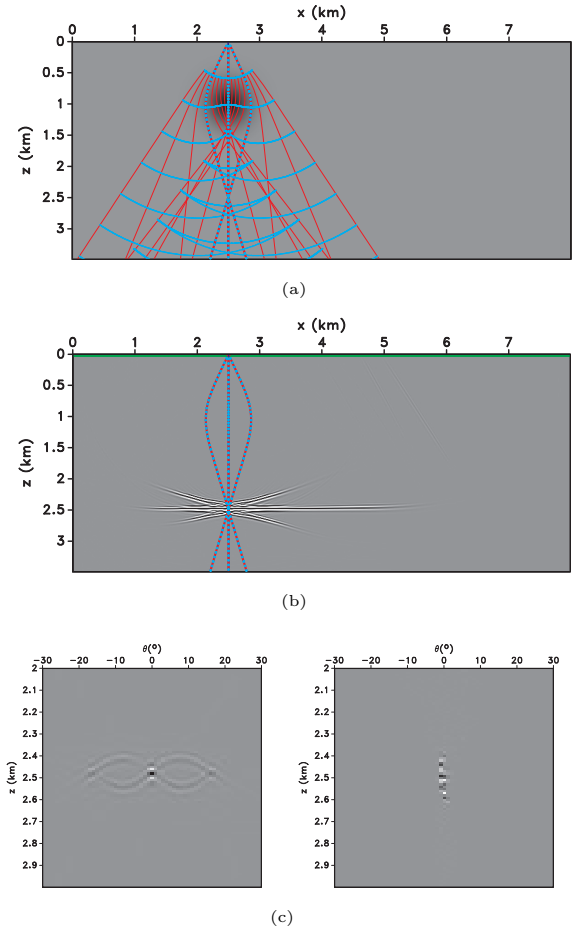

Figure 3: Simple synthetic illustrating angle-domain imaging with multi-pathing. The model (panel a) causes wavefield triplications which lead to multiple illumination paths in the image (panel b). The EI method captures all propagation paths (panel c, left) while the PV method does not (panel c, right).

trated in Figure 2. The figure shows the reflection angle calculations of both methods in a homogeneous isotropic model with a horizontal reflector for one shot at 5.5 km. Both methods output accurate reflection angles.

ALGORITHMS

We compare the two algorithms using the following criteria: wavefield reconstruction cost, imaging condition cost, angular resolution, ability to handle multipathing, robustness for reflectors with large curvature, and the ability to accurately describe anisotropic media.

1: The wavefield reconstruction step is computationally cheaper for the EI method than for the PV method because we do not require additional calculation of the particle velocity and PV components at each image point, at all times, and for all experiments. Algorithm 2 shows that the PV method requires both the pressure W and the particle velocity $\boldsymbol{V}$ fields, in contrast with the EI method which requires just the pressure field.

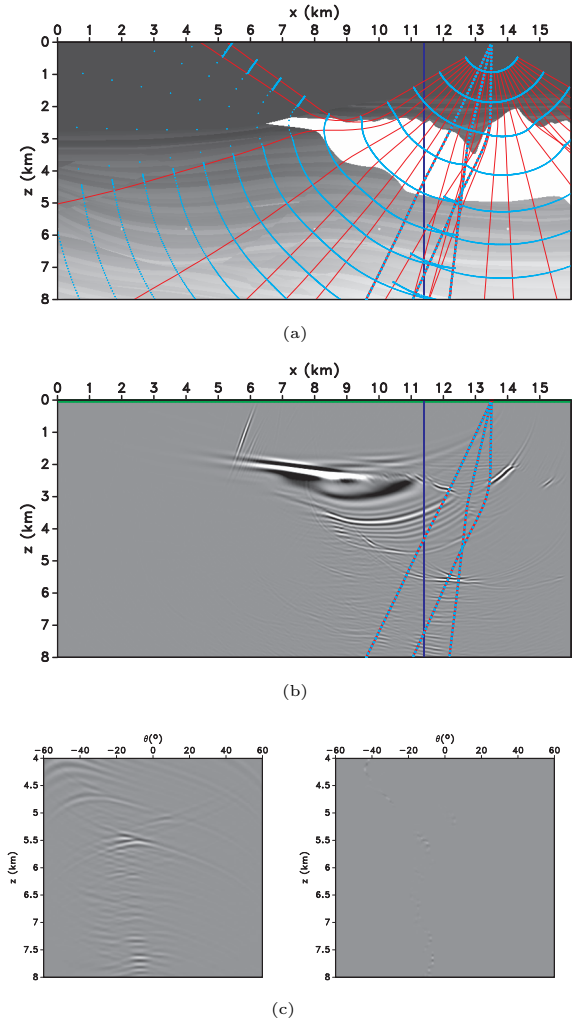

Figure 4: Synthetic example of complex geology. The model (panel a) contains a salt body causing wavefield triplications. These events result in a strong amplitude event in the image (panel b) and in artifacts in PV angle gathers (panel c, right). The EI method produces more reliable angle gathers (panel c, left).

2: The EI method is costlier due to the computation and storage of the additional cross-correlation lags which generate a larger-dimensional image $R(\mathbf{x}, \boldsymbol{\lambda})$. Even if we only compute the horizontal space-lags $\boldsymbol{\lambda} = \{\lambda_x, \lambda_y, 0\}$ at all locations, the output image is a 5D cube which requires longer access due to its increased size. The EI angle decomposition is performed after summation over experiments at an additional, albeit small, computational cost. In contrast, the PV method allows angle calculation at each grid point on the fly, as we propagate the wavefields in the medium. The PV method does not require computation of the additional cross-correlation

lags nor any additional conversions post-migration, although this cost savings are partially offset by the need to compute and store the local Poynting vectors at all positions and times. It appears, however, that the PV method requires fewer computational loops, thus potentially being more cost-effective for 3D angle decomposition.

3: The PV algorithm produces higher angular resolution because the method uses only local information at the image point (Dickens and Winbow, 2011). However, a complicated receiver wavefield makes it difficult to compute the receiver Poynting vector accurately (Yoon et al., 2011), which might lead to high-resolution but inaccurate angle-dependent reflectivity.

4: Another limitation of the PV method is that it assumes one dominant propagation direction for the source and receiver wavefields and therefore computes only one opening reflection angle. However, one reflection angle is not an accurate representation of the subsurface in complex geology where the wavefields are complicated by multipathing. Figures 3(a)-3(c) illustrate one such example. The model has a negative Gaussian anomaly which causes triplication of the wavefield, Figure 3(a). Migration of one single shot shows the effects of multipathing, i.e. multiple illumination angles at the reflection point, Figure 3(b). The EI and PV angle gathers displayed in Figure 3(c) show multiple (EI, left), or single (PV, right) illumination angles.

Algorithm 1 – EI angle decomposition

for e **do**
  for t,**x do**
    for $\boldsymbol{\lambda}$ **do**
      $R(\mathbf{x},\boldsymbol{\lambda}) += W_s(e,\mathbf{x}+\boldsymbol{\lambda},t)\,W_r(e,\mathbf{x}-\boldsymbol{\lambda},t)$
    end for
  end for
end for
for **x do**
  for θ,ϕ **do**
    $R(\mathbf{x},\boldsymbol{\lambda}) \longrightarrow R(\mathbf{x},\theta,\phi)$
  end for
end for

Algorithm 2 – PV angle decomposition

for e **do**
  for t,**x do**
    $\mathbf{P}_s(e,\mathbf{x},t) = W_s(e,\mathbf{x},t)\,\boldsymbol{V}_s(e,\mathbf{x},t)$
    $\mathbf{P}_r(e,\mathbf{x},t) = W_r(e,\mathbf{x},t)\,\boldsymbol{V}_r(e,\mathbf{x},t)$
    $\{\mathbf{P}_s,\mathbf{P}_r\}(e,\mathbf{x},t) \longrightarrow \{\theta,\phi\}(e,\mathbf{x},t)$
    $\{W_s,W_r\}(e,\mathbf{x},t) \longrightarrow R(\mathbf{x},\theta,\phi)$
  end for
end for

5: The EI method degrades if the imaged reflectors are characterized by high curvature or by rapid lateral velocity variation. In contrast, the PV method does not have similar constraints on reflector curvature because of the localized angle computation, although the local space and/or time smoothing degrades its ability to identify precise angles when the wavefields are too complex. Figures 4(a)-4(c) illustrate the behavior of the two angle-decomposition methods in complex geology similar to the one derived from the Sigsbee 2A model, Figure 4(a). The migrated image for one shot, Figure 4(b), shows the imprint of multipathing. This is also visible in the angle gathers shown in Figure 4(c). The EI method produces low-resolution angle gathers but captures the multipathing observed in this area. In contrast, the PV method produces high-resolution angle gathers but does not capture the wavefild multipathing and thus it does not correctly evaluate all incidence angles in the sub-salt region.

6: As demonstrated by Sava and Alkhalifah (2013), the EI method is applicable to wave-equation imaging in anisotropic media. This is mainly because this method exploits the wavefront geometry of the propagating wavefields, i.e. the gathers are related to the phase angles at the image points. In contrast, the PV method produces gathers related to the group angles which need to be converted to the phase angles (Dickens and Winbow (2011)).

CONCLUSIONS

We extract reflection and azimuth angles using the extended images (EI) and Poynting vector (PV) methods. Each method has its own advantages and applications. In simple models, the PV method produces high angular resolution and is less computationally intensive than the EI method. In areas characterized by multipathing, the PV method produces only one angle per image point and provides a less accurate representation of angle-dependent reflectivity. The PV components oscillate rapidly and are impacted by wavefield noise. Furthermore, in anisotropic media, PV angle decomposition is further complicated by the need to convert group to phase angles at each image point. The EI method is potentially costlier since it requires cross-correlation lags at all locations where angle decomposition is needed. Otherwise, the method accurately and simultaneously maps all reflections into the angle domain and is readily applicable to anisotropic media. However, lateral velocity variations or high reflector curvature reduce the accuracy of EI angle calculations.

ACKNOWLEDGMENTS

This work was supported by the sponsors of the Center for Wave Phenomena at Colorado School of Mines. The reproducible numeric examples in this paper use the Madagascar open-source software package freely available from http://www.ahay.org.

REFERENCES

Biondi, B., and W. Symes, 2004, Angle-domain common-image gathers for migration velocity analysis by wavefield-continuation imaging: Geophysics, **69**, 1283–1298.

Claerbout, J. F., 1985, Imaging the earth's interior: Blackwell Scientific Publications.

Crawley, S., N. D. Whitmore, A. Sosa, and M. Jones, 2012, Improving rtm images with angle gathers: SEG Technical Program Expanded Abstracts, 1–5.

de Bruin, C. G. M., C. P. A. Wapenaar, and A. J. Berkhout, 1990, Angle-dependent reflectivity by means of prestack migration: Geophysics, **55**, 1223–1234.

Dickens, T. A., and G. A. Winbow, 2011, Rtm angle gathers using poynting vectors: SEG Technical Program Expanded Abstracts, 3109–3113.

Fomel, S., 1997, Migration and velocity analysis by velocity continuation: Stanford Exploration Project Report, **92**, 159–188.

———, 2004, Theory of 3d angle gahters in wave-equation imaging: 74th Annual International Meeting, Society of Exploration Geophysicists, 1053–1056.

———, 2011, Theory of 3-d angle gathers in wave-equation seismic imagine: Journal of Petroleum Exploration and Production Technology, **1**, 11–16.

Gray, S., J. Etgen, J. Dellinger, and D. Whitmore, 2001, Seismic migration problems and solutions: Geophysics, **66**, 1622–1640.

Kaufman, A. A., A. L. Levshin, and K. L. Larner, 2002, Acoustic and elastic wave fields in geophysics, part ii: Elsevier, **37**.

Prucha, M., B. Biondi, and W. Symes, 1999, Angle-dependent common image gathers by wave-equation migration: SEG Technical Program Expanded Abstracts, 824–827.

Rickett, J. E., and P. C. Sava, 2002, Offset and angle-domain common image-point gathers for shot-profile migration: Geophysics, **67**, 883–889.

Sava, P., and T. Alkhalifah, 2013, Wide-azimuth angle gathers for anisotropic wave-equation migration: Geophysical Prospecting, **61**, 75–91.

Sava, P., and I. Vasconcelos, 2011, Extended imaging condition for wave-equation migration: Geophysical Prospecting, **59**, 35–55.

Sava, P., and I. Vlad, 2011a, Wide-azimuth angle gathers for wave-equation migration: Geophysics, **76**, S131–S141.

———, 2011b, Wide-azimuth angle gathers for wave-equation migration: Geophysics, submitted for publication.

Sava, P. C., B. Biondi, and S. Fomel, 2001, Amplitude-preserved common image gathers by wave-equation migration: 71st Annual International Meeting, Society of Exploration Geophysicists, 296–299.

Sava, P. C., and S. Fomel, 2000, Angle-gathers by fourier transform: Stanford Exploration Project Report, **103**, 119–130.

———, 2003, Angle-domain common-image gathers by wavefield continuation methods: Geophysics, **68**, 1065–1074.

———, 2005, Coordinate-independent angle-gathers for wave equation migration: SEG Technical Program Expanded Abstracts, 2052–2055.

Vyas, M., D. Nichols, and E. Mobley, 2011, Efficient rtm angle gathers using source directions: SEG Technical Program Expanded Abstracts, 3104–3108.

Yoon, K., M. Guo, J. Cai, and B. Wang, 2011, 3d rtm angle gathers from source wave propagation direction and dip of reflector: SEG Technical Program Expanded Abstracts, 3136–3140.

Yoon, K., and K. Marfurt, 2004, Challenges in reverse-time migration: SEG Technical Program Expanded Abstracts, 1057–1060.